Determination of the interfacial cohesive material law for SRG composites bonded to a masonry substrate

Determination of the interfacial cohesive material law for SRG composites bonded to a masonry substrate

Mattia Santandrea[1], Francesco Focacci[2], Claudio Mazzotti[3], Francesco Ubertini[4], and Christian Carloni[5*]

[1] *Department of Civil, Chemical, Environmental, and Materials Engineering, University of Bologna, Viale Risorgimento 2, 40126 Bologna, Italy, mattia.santandrea3@unibo.it, +39 051-209-3375*

[2] *eCampus University, Via Isimbardi 10, 22060, Novedrate, CO, Italy, francesco.focacci@uniecampus.it*

[3] *Department of Civil, Chemical, Environmental, and Materials Engineering, University of Bologna, Viale Risorgimento 2, 40126 Bologna, Italy, claudio.mazzotti@unibo.it, +39 051-209-3251*

[3] *Department of Civil, Chemical, Environmental, and Materials Engineering, University of Bologna, Viale Risorgimento 2, 40126 Bologna, Italy, francesco.ubertini@unibo.it, +39 051 209 9942*

[5] *Department of Civil Engineering, Case Western Reserve University, 10900 Euclid Avenue Cleveland OH U.S.A., christian.carloni@case.edu, +1-216-368-4193*

Abstract

Fiber reinforced cementitious matrix (FRCM) composites, also known as textile reinforced matrix (TRM) composites, are a suitable alternative to fiber reinforced polymer (FRP) composites to strengthen reinforced concrete and masonry structures. In the toolbox of FRCMs, a recently-developed composite that employs high-strength steel fibers embedded in a hydraulic mortar is particular appealing for applications on historical masonry constructions. This type of composite is known as steel reinforced grout (SRG). In this paper, an extensive experimental work is presented. Single-lap shear tests are performed to study the debonding of SRG strips from a masonry substrate, which is the critical failure mode for strengthening applications. For SRGs, debonding typically occurs at the fiber-matrix interface.

* Corresponding Author

A large scatter of the experimental results is observed, which is related to the variability of hydraulic mortars and their ability to impregnate the fibers. Although strain gauges can be applied directly to the fibers to obtain the experimental strain profile along the fibers, because of the presence of the matrix these measurements are complex and in some cases not reliable. Thus, indirect method based on the global response of the test is proposed to obtain the interfacial properties.

Key words: SRG, Debonding, Cohesive Material Law, Masonry

1. Introduction

Strengthening solutions to rehabilitate existing masonry buildings have always attracted the interest of the scientific community since they allow to preserve historical constructions through an understanding of the original structural configuration. Strengthening applications are useful to guarantee safety of a damaged or deficient structure and are considered a sustainable choice to avoid the demolition of existing buildings. In the last decades, strengthening solutions gained a renewed interest due to the seismic events that hit several European countries (Italy, Greece, and Turkey). Natural hazards, such as earthquakes, have shown the inadequacy of certain masonry structures to withstand horizontal loads, and brought up the need for an adequate strengthening intervention to avoid certain collapse mechanisms of the structure. In the last 30 years, new strengthening systems, such as fiber reinforced polymer (FRP) composites, have been employed to avoid the onset of a collapse mechanism of some structural components of the construction and increase the load-carrying capacity [1-3]. Several researchers conducted experimental campaigns to investigate the debonding mechanism of FRP systems bonded to a masonry substrate [3-11]. It was observed that failure usually occurred in the masonry substrate and was characterized by a cohesive crack that propagated both in the bricks and in the mortar joints. Despite FRP systems are able to enhance the load-carrying capacity of a masonry structure, they feature several disadvantages when applied to existing structures, such as the poor behavior at elevated temperatures and lack of reversibility

of the application. In addition, FRP composites have a low vapor compatibility with masonry substrates. In an attempt to overcome the disadvantages of traditional FRP systems, a new family of composites, known as fiber reinforced cementitious matrix (FRCM) or textile-reinforced mortar (TRM) composites, was recently developed. FRCM composites consist of high-strength fibers embedded within an inorganic matrix. FRCM systems were firstly employed in the late 1990s in new concrete constructions [12-14], while from the early 2000s they were employed for strengthening applications as external flexural and shear reinforcement of reinforced concrete beams [15-19] and for confinement [20] of concrete. FRCM composites offer several advantages when compared to traditional FRPs: 1) high resistance to fire and high temperatures; 2) resistance to UV radiation; 3) ease of handling during the application because the inorganic binder is water-based; 4) permeability compatible with concrete and masonry substrates; and 5) unvarying workability time (between 4°C and 40°C) [21]. FRCM composites proved to be effective also in the field of strengthening of masonry structures [22-29]. Experimental tests on FRCM composites bonded to a masonry substrate have been also reported in the literature, using carbon, polyparaphenylene benzobisoxazole (PBO), glass or basalt fibers [30-35]. Experimental results have shown that the typical failure of FRCM composites bonded to a masonry substrate consisted in the rupture of the fibers or in the delamination at the fiber-matrix interface. Newly-developed high-strength steel fibers were recently employed in FRCM systems and are referred to as steel reinforced grout (SRG) composites. SRG composites consist of high-strength steel fibers embedded in a cementitious or lime-based grout. The low cost of the steel fibers compared to carbon or aramid fibers and the possibility to apply steel fibers also to sharp corners of masonry and concrete structures [36-37] determined the success of this new strengthening system. Despite the available studies carried out to investigate the bond behavior of SRG-masonry joints [38-40] and of SRG-brick interfaces [41-42], which highlighted the effectiveness of this strengthening system, some important aspects of the SRG-masonry debonding mechanism are still not fully investigated. For example, the definition of the cohesive material law (CML) [43], i.e. the local relationship between the shear stress and the slip (fiber-substrate relative displacement), is a key property

of the interface as it allows to determine important design parameters, such as the bond capacity and the effective bond length.

This work presents the result of an extensive experimental campaign designed to study the bond mechanism of SRG-masonry joints. Single-lap shear tests are performed. Length of the bonded area and loading rate of the tests are varied. An indirect method is then used to determine the interfacial cohesive material law that describes the debonding phenomenon [44].

2. Experimental Program

Single-lap shear tests were performed using a push-pull configuration, shown in Figure 1, to study the bond behavior of SRG composites applied to a masonry substrate.

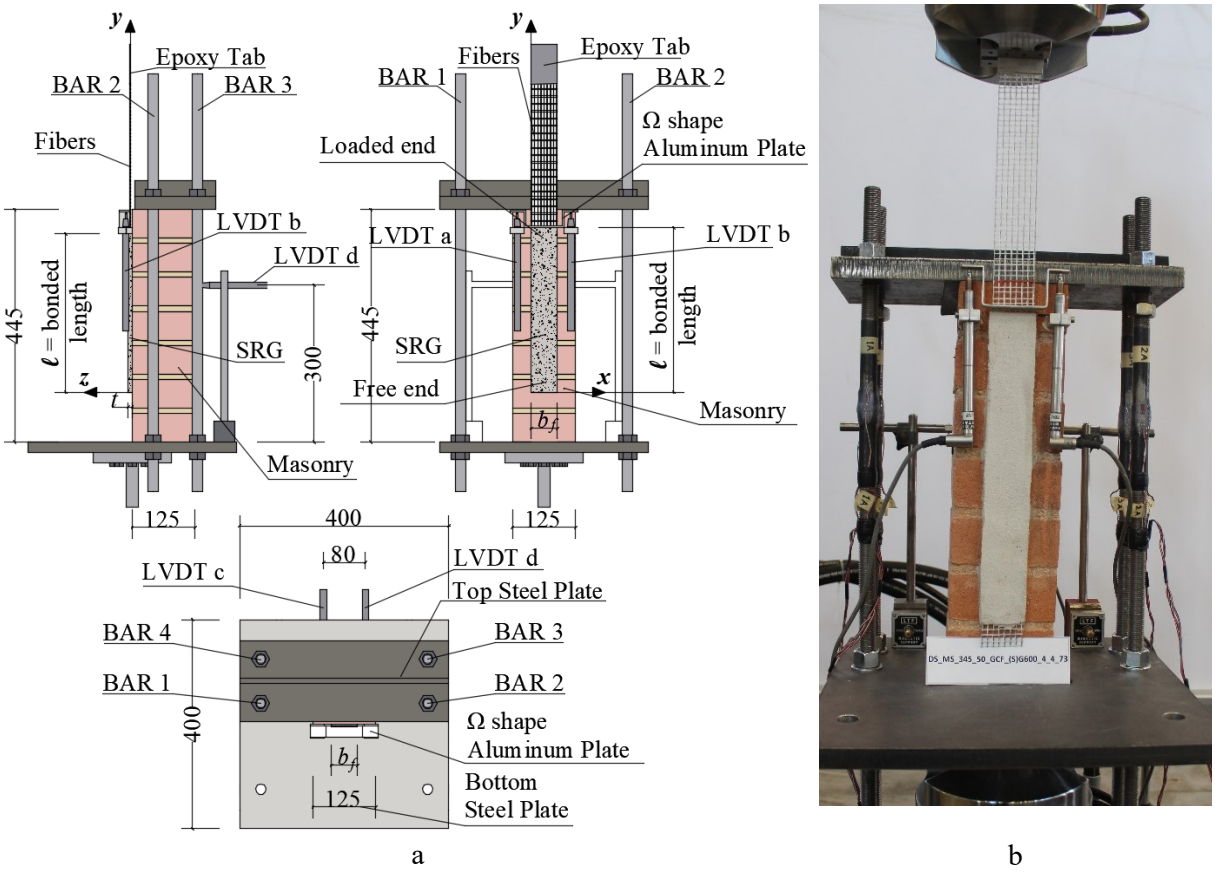

Figure 1. Single-lap shear test setup: sketch (a) and photo of a representative specimen (b).

2.1 Materials

All the masonry blocks employed in this experimental campaign were constructed with solid clay bricks and a low strength mortar. Twenty cylinders were cored from five half-bricks extracted from the masonry blocks after the direct shear tests were performed. The nominal dimensions of the cylinders were 50 mm (*diameter*) × 50 mm (*length*). Out of twenty cylinders, seven were used to determine the tensile strength of bricks, f_{bt}, through splitting tests (Figure 2a), while thirteen were used to evaluate the compressive strength of bricks, f_{bc}, according to [45] (Figure 2b).

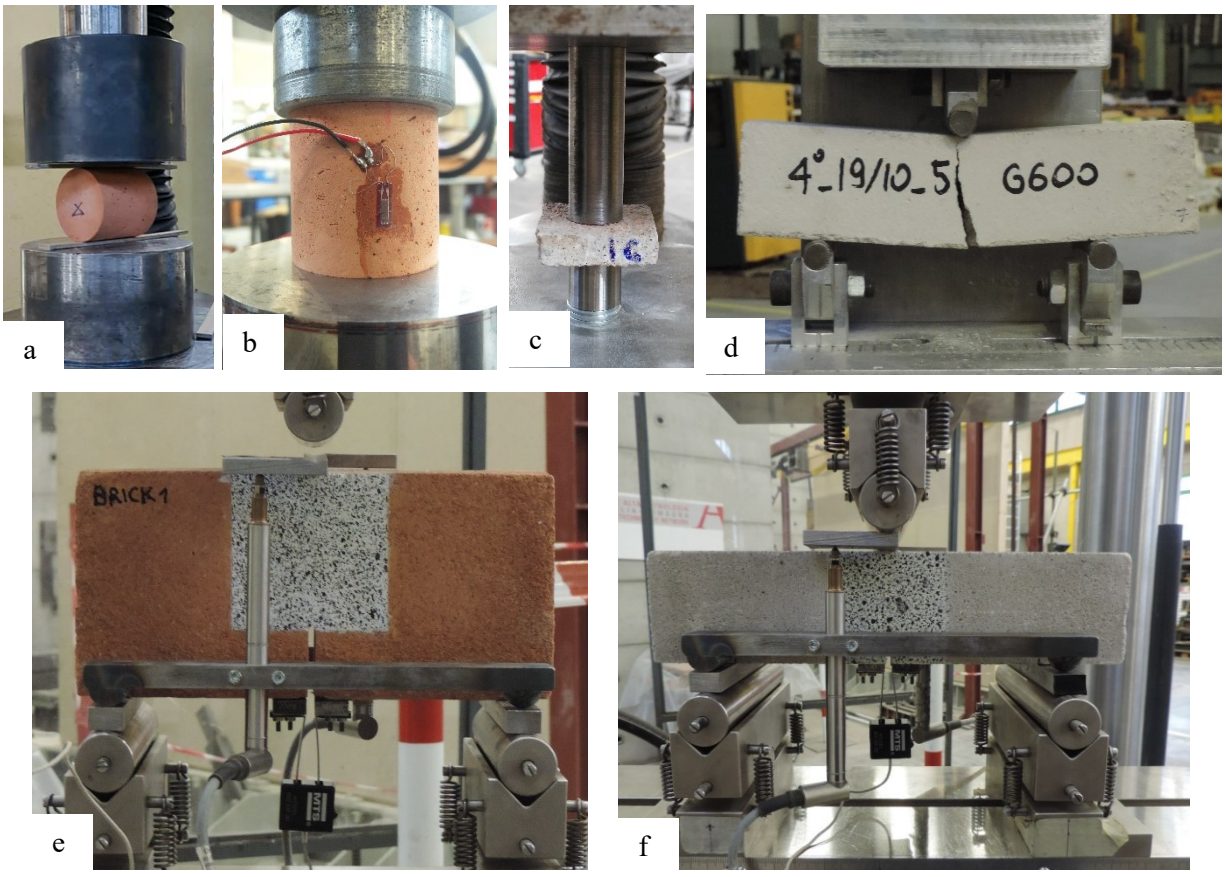

Figure 2. Material characterization: a) splitting test on a cylinder cored from a half brick; b) compression test on a cylinder cored from a half brick; c) Double punch test on a mortar joint; d) Three-point bending (TPB) test on a matrix mortar prism; e) Fracture mechanics test on a notched brick; f) Fracture mechanics test on a notched matrix mortar prism.

The splitting tensile strength of bricks, f_{bt}, resulted equal to 3.12 MPa (CoV 0.12), while the compressive strength of bricks, f_{bc}, resulted equal to 20.3 MPa (CoV 0.17). Out of the thirteen cylinders tested in compression, five were instrumented with two strain gages applied at mid-height of the specimen and arranged 180° apart one another to measure the longitudinal strain. The average strain calculated from the measurements of the two strain gages was used to evaluate the elastic modulus of the bricks, E_b, assumed as the slope of stress-strain response between the 5% and the 30% of the peak stress. The elastic modulus of the bricks, E_b, resulted equal to 7.3 GPa (CoV 0.29). In addition, fracture mechanics tests were performed using a three-point bending test set-up [46] on three 250 mm length (L) × 55 mm width (b) × 120 mm depth (d) notched bricks, selected from the group of bricks employed to construct the masonry blocks (Figure 2e). The fracture energy of each brick was evaluated as the area under the load-deflection response (Figure 3a) divided by the area of the ligament [47-49] and the average value of the fracture energy resulted equal to 34 N/m (CoV 0.16). Double punch tests were performed according to [50] on fourteen mortar joint samples extracted from the masonry blocks after single-lap shear tests were performed (Figure 2c). The compressive strength of mortar joints obtained from double punch tests, f_m, resulted equal to 15.9 MPa (CoV = 0.20) [51].

The SRG composite applied to the masonry substrate consisted of high-strength steel fibers embedded in a lime-based hydraulic mortar (matrix). The steel fibers (cords) were in the form of a unidirectional sheet made of high-strength galvanized twisted steel micro-cords (filaments) held together by a glass fiber micro-mesh. Each cord consisted of five filaments. Three of the five filaments were straight, and the remaining two filaments were wrapped around the other three with a high torque angle. The cross-sectional area of the cord was 0.538 mm^2. Low density (LD) steel fibers with an equivalent thickness, $t^*_{f,\mathrm{LD}}$, equal to 0.084 mm were used in this experimental work. The physical and mechanical properties of the steel fibers provided by the manufacturer [52] are reported in Table 1.

Ten batches of the lime-based matrix mortar were used to strengthen the masonry blocks. Out of the ten batches, the matrix mortar of four batches was characterized by performing fracture mechanics tests and/or flexural and compressive tests on mortar specimens cast with the same mortar used to strengthen

the masonry blocks. The four different batches are referred to as B1, B2, B3, and B4. Flexural and compressive tests were performed on 40 mm × 40 mm × 160 mm mortar prisms according to [53] (Figure 2d). Fracture mechanics tests were performed on 300 mm length (L) × 70 mm width (b) × 70 mm depth (d) notched matrix prisms using the same test set-up adopted for bricks (Figure 2f and Figure 3b). The average value of the Mode-I fracture energy of the matrix mortar, $G_{F,m}^{I}$, the flexural strength, f_{mt}, and the compressive strength, f_{mc}, are reported in Table 2 for the four mortar batches considered. As a reference, the flexural strength, f_{mt}, and the compressive strength, f_{mc}, as reported by manufacturer, resulted equal to 5 MPa and 15 MPa, respectively. The 300 mm × 70 mm ×70 mm notched matrix mortar prisms, the 40 mm × 40 mm × 160 mm mortar prisms, cast from the four batches of mortar described above and employed to characterize the matrix of the SRG system, as well as the composite strips were cured under wet cloths for 28 days.

Table 1. Properties of the steel fibers (textile) provided by manufacturer [52]

Property	Low Density
Number of Cords/mm	0.157
Tensile Strength, $f_{f,u}^{\mathrm{A}}$ [MPa]	$f_{f,u}^{\mathrm{LD}} > 3000$
Elastic Modulus, E_f [GPa]	> 190
Ultimate Strain, ε_{fu} [%]	> 2
Equivalent Thickness, $t_{f,\mathrm{A}}^{*}$ [mm]	$t_{f,\mathrm{LD}}^{*} \approx 0.084$

Note: $f_{f,u}^{\mathrm{A}}$ is the tensile strength of the fibers. $t_{f,\mathrm{A}}^{*}$ is the equivalent thickness of the fibers. Superscript A=LD represents the steel fiber density (low density).

Table 2. Mechanical properties of the matrix mortar

Batch of mortar	Fracture energy, $G_{F,m}^{I}$ [N/m]	Compressive strength, f_{mc} [MPa]	Flexural strength, f_{mt} [MPa]
B1	39 (0.21)	15*	5*
B2	/	10.70 (0.03)	3.02 (0.08)
B3	30	15.7 (0.04)	5.87 (0.13)
B4	29	11.3 (0.07)	5.18 (0.08)

* These values of the compressive strength, f_{mc}, and flexural strength, f_{mt}, of the matrix mortar were obtained from the technical data sheet provided by the manufacturer [52]. For some mortar batches, the amount of mortar was not sufficient to cast all the additional specimens for material characterization.

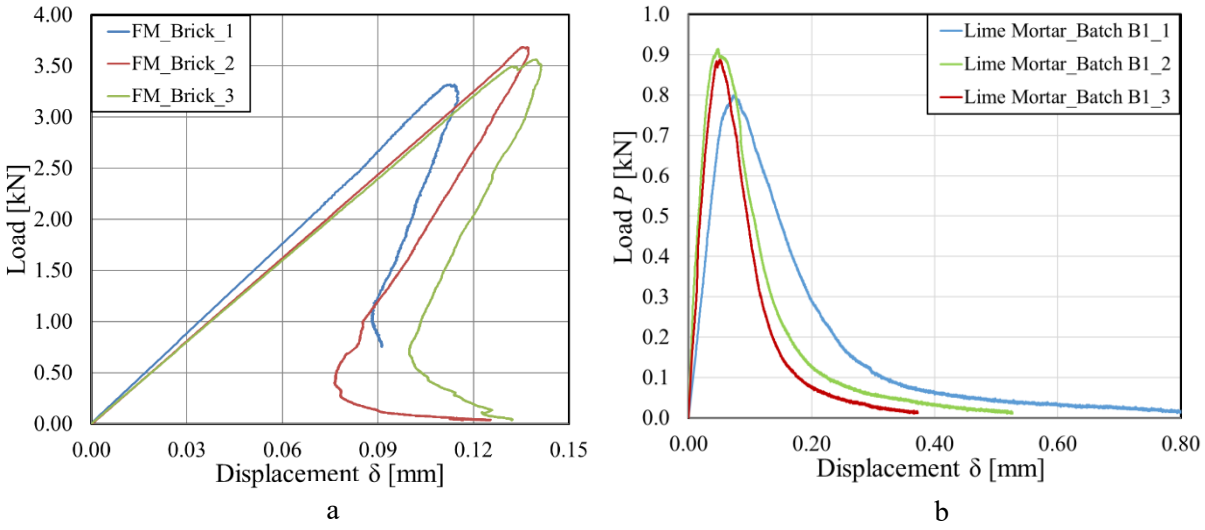

Figure 3. Load-displacement response obtained from fracture mechanics tests performed on notched bricks (a) and notched matrix mortar prisms (b).

2.2 Specimen description and preparation

Seventy-eight SRG-masonry joints were tested using a single-lap shear test set-up (Figure 1). The parameters investigated in this experimental work were the bonded length (from 100 mm to 345 mm) and the test rate (0.00084 mm/s and 0.0084 mm/s). SRG composites were externally bonded to one face of the masonry blocks. The nominal dimensions of all masonry blocks were equal to 120 mm × 120 mm × 445 mm, i.e. each block consisted of 7 half bricks and 6 10 mm-thick mortar joints. Prior to applying the SRG strip, the faces of each specimen were wetted by soaking completely each masonry block in a bucket of water for twenty minutes. The water immersion of each specimen (Figure 4a) was needed to avoid water absorption by the masonry surface during the application of the composite strip. Three phases can be identified during the application of the SRG composite strip: 1) application of the first layer of matrix mortar on the designated bonded area of the masonry block (Figure 4b and c); 2) the steel fiber sheet is placed on top of the first layer of mortar and gently pressured against it in order to guarantee the impregnation of the fibers (Figure 4d); 3) application of the external layer of matrix mortar in order to cover completely the fiber sheet (Figure 4e). After the application of the second layer of matrix, SRG strips were cured for 28 days under wet cloths. The bonded width, b_f, was maintained constant for all specimens and was equal to 50 mm. All the fiber sheets were comprised of 8 cords. The cords were arranged across the width of the SRG strip in order to have approximatively a distance between the external cords of the fiber sheet and the edges of the matrix mortar equal to half of the fiber spacing. Both the internal and the external layer of matrix had a thickness equal to 4 mm, which in turn corresponded to a total thickness of the SRG composite strip equal to 8 mm. Fibers were left bare outside the bonded area, i.e. the matrix was only used in the bonded area. The length of the bare fiber portion of the SRG strip was 335 mm for all specimens. A 75 mm-long epoxy tab was constructed with a thermosetting epoxy at the end of the fiber strip and used to facilitate the gripping of the fibers by the jaws of the testing machine. The bonded area started 35 mm from the edge of the masonry block in order to avoid spalling of the first brick of the block. Specimens with eleven different bonded lengths were tested, i.e. 75 mm, 100 mm, 125 mm, 150 mm, 175 mm, 200 mm, 215 mm, 250 mm, 280 mm, 315 mm, and 345 mm.

Specimens were named following the notation DS_X_Y_A_B_C_D_Z, where X = bonded length (ℓ) in mm; Y = bonded width (b_f) in mm; A represents the steel fiber density (LD = low density); B indicates the type of matrix (LM = lime-based mortar); C (if present) denotes the batch of mortar (B1, B2, B3 or B4); D (if present) indicates the test rate was different from the standard rate (0.00084 mm/s) used for the majority of the specimens (10R = ten times the standard rate); and Z = specimen number (Table 3).

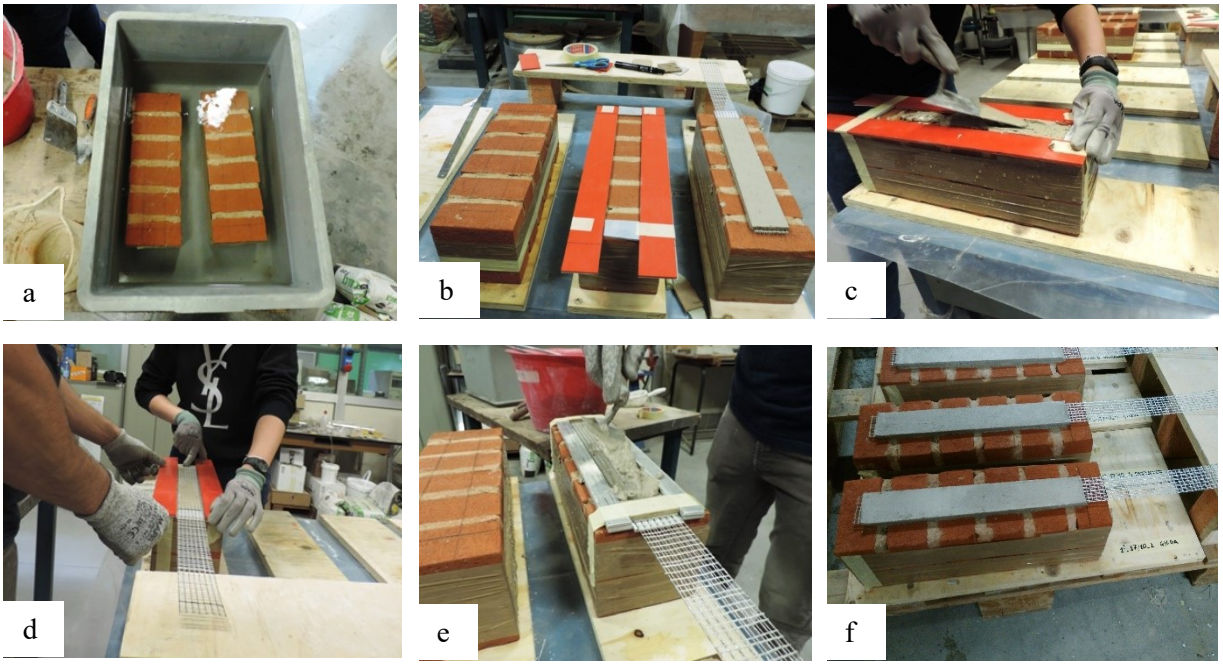

Figure 4. Application of the SRG composite to the masonry block: a) water immersion of the masonry block; b) definition of the bonded area; c) application of the internal layer of matrix mortar; d) application of the steel fiber sheet; e) application of the external layer of matrix mortar; f) SRG-masonry joint after the curing period under wet cloths.

2.3 Test procedure

Seventy-eight single-lap shear tests were performed in this experimental campaign. Direct single-lap shear tests were conducted under displacement control using a closed-loop servo-hydraulic universal testing machine with a capacity of 100 kN. The classical push-pull configuration was adopted, i.e. the masonry block was restrained against movements by two steel plates while fibers were pulled. The sketch and a photo of the test set-up is shown in Figure 1. A cylindrical steel element, fixed to the bottom square plate, was directly clamped by the bottom jaws of the testing machine. The bottom steel plate and the top rectangular steel plate were connected by four steel bars through bolts. On each steel bar, three strain gages were mounted. The strain gages were aligned with the longitudinal axis of the bar and were arranged 120° apart one another. The average value of the three strain measurements on each bar, was used to evaluate the strain of the bar and consequently the pre-stressing load applied to the masonry block prior to starting the single lap-shear test. The same pre-stressing load (approximately 1 MPa) was applied to all the specimens at the beginning of the test and the stress along each bar was monitored during the test. Thin neoprene sheets were placed in between the square faces of the masonry block and the steel plates, in order avoid any stress concentration.

Two LVDTs (LVDT a and LVDT b) were mounted on the masonry surface close to the beginning of the bonded area (loaded end). The LVDTs reacted off of a thin aluminum Ω-shaped plate that was glued directly to the bare fibers at the loaded end of the SRG strip. The average value of the LVDT measurements is referred to as global slip, g, in this paper and was used to control the test at a constant rate equal to 0.00084 mm/s, which has been considered as the standard rate in other experimental campaigns conducted by the authors [54]. Out of the 78 specimens, 3 specimens were tested with a rate equal to 0.0084 mm/s, i.e. ten times the standard rate. Two additional LVDTs (LVDT c and LVDT d) were mounted against the face of the masonry block opposite to the surface where the SRG strip was applied, and were used to monitor the horizontal displacements of the masonry block. LVDT c and LVDT d were fixed to the bottom plate by means of two magnets. All specimens were arranged 1 mm forward with respect to the position corresponding to the vertical alignment of the fibers with the machine grips. This expedient was used to balance the inevitable initial backward rotation of the block due to the

deformation of the mortar joints and the adjustment of the test fixture and it allowed the fibers to remain almost aligned with the top grips of the testing machine for the entire duration of the single-lap shear test.

Table 3. Test results of single-lap direct shear tests

Specimen Name	Bonded length [mm]	g_1 [mm]	g_2 [mm]	P^* [kN]	P_{crit} [kN]	$\overline{P_{crit}}$ [kN]	Failure mode	$\overline{w_c}$ [mm]	$\overline{w_d}$ [mm]
DS_75_50_LD_LM_1	75	\	\	4.70	\		MM	\	\
DS_75_50_LD_LM_2	75	\	\	2.98	\		MM	\	\
DS_75_50_LD_LM_3	75	\	\	3.38	\	\	MM	\	\
DS_75_50_LD_LM_4	75	\	\	3.84	\		MM	\	\
DS_100_50_LD_LM_1	100	\	\	2.97	\		MM	\	\
DS_100_50_LD_LM_2	100	\	\	4.03	\		MM	\	\
DS_100_50_LD_LM_3	100	\	\	7.26	\	\	MM	\	\
DS_100_50_LD_LM_4	100	\	\	5.65	\		MM	\	\
DS_125_50_LD_LM_1	125	\	\	4.41	\		MF	\	\
DS_125_50_LD_LM_2	125	\	\	6.44	\		MF	\	\
DS_125_50_LD_LM_3	125	\	\	8.08	\	\	MF	\	\
DS_125_50_LD_LM_4	125	\	\	6.20	\		MF	\	\
DS_125_50_LD_LM_5	125	\	\	7.12	\		MF	\	\
DS_150_50_LD_LM_1	150	\	\	6.23	\		MF	\	\
DS_150_50_LD_LM_2	150	\	\	4.53	\		MF	\	\
DS_150_50_LD_LM_3	150	\	\	3.58	\	\	MF	\	\
DS_150_50_LD_LM_4	150	\	\	4.97	\		MF	\	\
DS_175_50_LD_LM_1	175	1.05	1.65	7.74	6.81		MF	0.67	0.83
DS_175_50_LD_LM_2	175	\	\	5.80	\		MM/MF	\	\
DS_175_50_LD_LM_3	175	1.27	1.49	7.76	6.85	6.30	MF	1.01	0.94
DS_175_50_LD_LM_4	175	1.20	1.50	8.12	7.08		MF	1.63	1.76
DS_175_50_LD_LM_5	175	1.20	1.98	9.04	7.35		MF	1.77	1.78

DS_175_50_LD_LM_6	175	0.62	0.67	6.22	5.75		MF	1.37	1.42
DS_175_50_LD_LM_7	175	\	\	10.44	\		SF/MM	\	\
DS_175_50_LD_LM_8	175	0.84	1.04	5.30	3.97		MF	0.87	1.04
DS_175_50_LD_LM_9	175	\	\	5.44	\		MF	\	\
DS_175_50_LD_LM_10	175	\	\	8.34	\		MM	\	\
DS_200_50_LD_LM_1	200	0.58	1.16	7.28	5.64		MF	1.08	1.59
DS_200_50_LD_LM_2	200	\	\	8.80	\	5.57	MF	\	\
DS_200_50_LD_LM_3	200	0.48	1.06	6.04	5.50		MF	1.30	1.42
DS_215_50_LD_LM_1	215	\	\	13.15	\		FR	\	\
DS_215_50_LD_LM_2	215	\	\	13.20	\	\	FR	\	\
DS_215_50_LD_LM_3	215	\	\	12.84	\		MF	\	\
DS_250_50_LD_LM_B2_1	250	0.70	1.57	7.06	6.16		MF	0.39	0.49
DS_250_50_LD_LM_B2_2	250	0.40	1.30	5.06	4.71		MF	0.91	1.10
DS_250_50_LD_LM_B2_3	250	0.61	1.48	5.42	4.67	4.95	MF	2.29	2.33
DS_250_50_LD_LM_B2_4	250	0.60	1.33	5.70	5.60		MF	1.45	1.23
DS_250_50_LD_LM_B2_5	250	0.39	0.62	4.68	3.64		MF	1.94	1.87
DS_280_50_LD_LM_1	280	\	\	10.88	\		MF	\	\
DS_280_50_LD_LM_2	280	\	\	7.81	\	4.92	MF	\	\
DS_280_50_LD_LM_3	280	\	\	9.25	\		MF	\	\
DS_280_50_LD_LM_4	280	0.75	1.59	5.92	4.92		MF	0.68	0.70
DS_315_50_LD_LM_B2_1	315	0.73	1.30	7.49	5.27		MF	1.69	1.44
DS_315_50_LD_LM_B2_2	315	\	\	12.75	\		FR	\	\
DS_315_50_LD_LM_B2_3	315	\	\	6.21	\		MF	\	\
DS_315_50_LD_LM_B2_4	315	1.00	2.30	6.78	6.33		MF	1.51	1.79
DS_315_50_LD_LM_5	315	\	\	5.05	\		MF	\	\
DS_315_50_LD_LM_6	315	1.03	2.49	7.76	6.85	6.22	MF	1.60	1.69
DS_315_50_LD_LM_7	315	1.54	2.35	7.83	6.67		MF	1.22	1.39
DS_315_50_LD_LM_8	315	1.12	2.22	7.52	5.84		MF	0.92	1.15
DS_315_50_LD_LM_9	315	\	\	6.50	\		MF	\	\
DS_315_50_LD_LM_10	315	0.58	1.92	5.88	5.48		MF	1.74	1.66
DS_315_50_LD_LM_11	315	1.18	2.29	6.36	5.84		MF	1.14	0.99

DS_315_50_LD_LM_12	315	1.90	2.30	7.79	7.50		MF	1.47	1.34
DS_315_50_LD_LM_B3_13	315	1.33	2.18	6.07	5.75		MF	1.25	1.40
DS_315_50_LD_LM_B3_14	315	\	\	11.40	\		MF	\	\
DS_315_50_LD_LM_B4_15	315	1.15	2.26	8.12	6.65		MF	0.80	0.94
DS_315_50_LD_LM_B1_10R_1	315	\	\	8.46	\		MF	\	\
DS_315_50_LD_LM_B1_10R_2	315	\	\	10.31	\		MF	\	\
DS_315_50_LD_LM_B1_10R_3	315	\	\	12.46	\		MF	\	\
DS_345_50_LD_LM_1	345	\	\	9.85	\		MF	\	\
DS_345_50_LD_LM_2	345	\	\	11.26	\		MF	\	\
DS_345_50_LD_LM_3	345	1.25	2.90	9.17	8.53		MF	2.80	2.99
DS_345_50_LD_LM_4	345	0.97	1.62	9.56	8.84		MF	1.45	1.54
DS_345_50_LD_LM_5	345	\	\	12.30	\		MF	\	\
DS_345_50_LD_LM_6	345	\	\	11.74	\		FR (1)	\	\
DS_345_50_LD_LM_7	345	\	\	10.18	\		MF	\	\
DS_345_50_LD_LM_8	345	1.17	2.44	7.06	6.42		MF	1.43	1.41
DS_345_50_LD_LM_9	345	\	\	13.14	\	7.91	FR (1)	\	\
DS_345_50_LD_LM_10	345	\	\	13.18	\		FR (1)	\	\
DS_345_50_LD_LM_11	345	0.54	2.87	9.05	8.47		MF	0.89	0.79
DS_345_50_LD_LM_12	345	0.64	1.11	7.15	6.31		MF	1.08	1.04
DS_345_50_LD_LM_13	345	1.02	2.18	10.75	8.96		MF	1.37	1.55
DS_345_50_LD_LM_14	345	0.91	1.38	7.98	7.38		MF	1.13	1.13
DS_345_50_LD_LM_15	345	\	\	12.22	\		MF	\	\
DS_345_50_LD_LM_16	345	\	\	10.30	\		MF	\	\
DS_345_50_LD_LM_17	345	1.65	2.82	9.25	8.33		MF	1.82	1.81
DS_345_50_LD_LM_18	345	\	\	8.59	\		MF	\	\

3. Load responses and failure modes

This section reports the results of 78 single-lap shear tests performed on SRG-masonry joints in terms of load response (relationship between the applied load P and the global slip g) and failure mode.

The applied load P versus global slip g response (or simply load response) of representative specimens are presented in Figure 5a for different bonded lengths. The shape of the load response was affected by the bonded length of the SRG strip and by the failure mode.

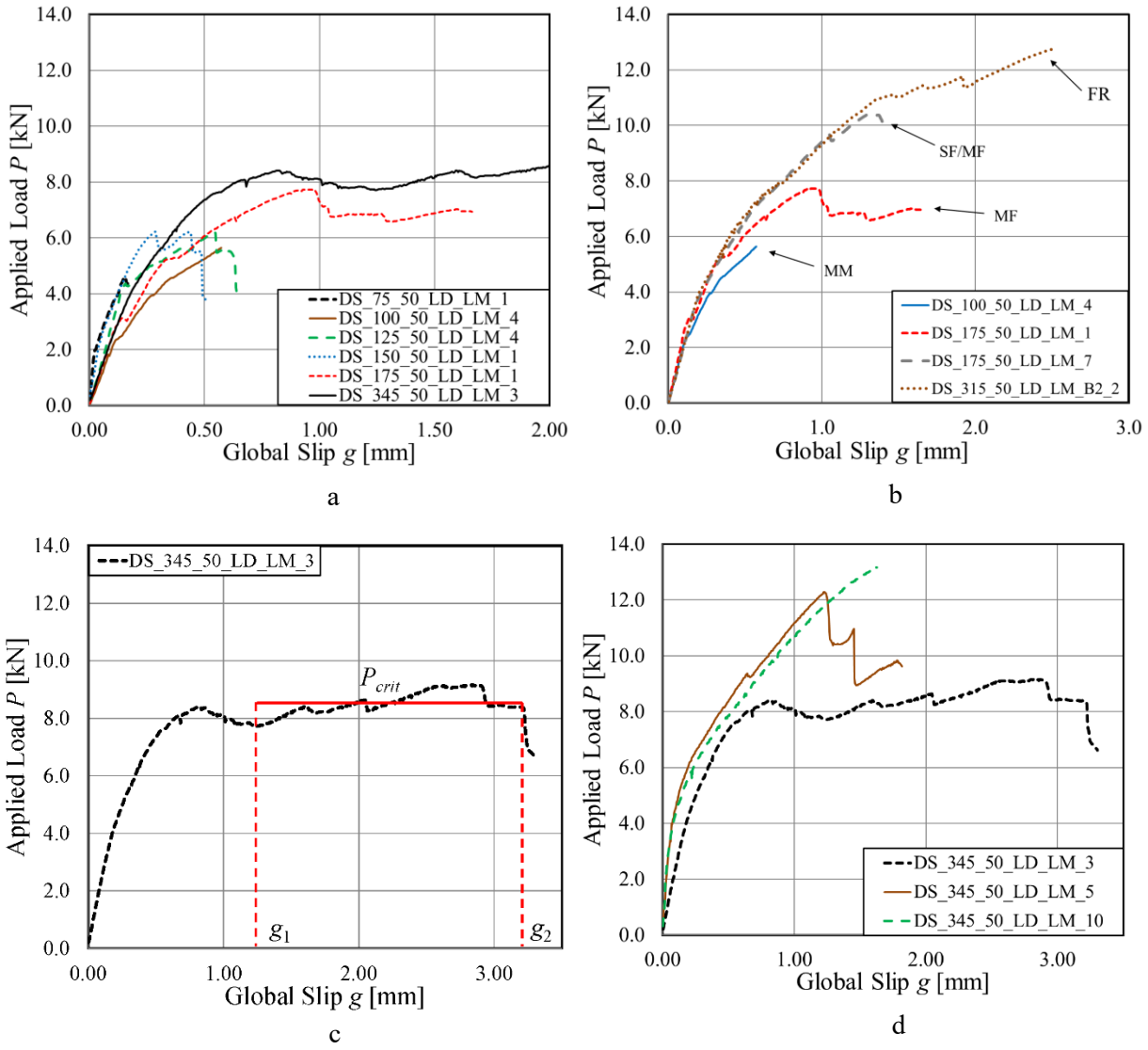

Figure 5. a) Representative load responses for different bonded length; b) Representative load responses for different failure modes, c) Load response of specimen DS_345_50_LD_LM_3; d) Representative load responses for ℓ =345 mm.

Four different failure modes were observed (Figure 6): a) debonding of the SRG strip at the matrix-masonry interface (MM) (Figure 6a), b) interlaminar failure at the matrix-fiber interface (MF)(Figure 6b), c) rupture of the steel fibers (FR) (Figure 6c), and d) mixed failure mode (SF/MF) characterized by the detachment of the SRG strip from the substrate with a thin layer of masonry attached to it (SF) in a limited portion of the bonded region and by the interlaminar failure (MF) in the remaining portions of the bonded region (Figure 6d). It should be observed that type d) failure was observed only for specimen DS_175_50_LD_LM_7 (Figure 5b).

For all specimens, the load response was characterized by an initial linear branch followed by a non-linear portion until the peak load, P^*, was reached. Specimens with a bonded length equal to or lower than 150 mm failed as the peak load was reached. The failure mode for specimens with a bonded length ℓ equal to 75 mm and 100 mm was always type a), i.e. MM, while the failure mode for specimens with ℓ = 125 mm and ℓ = 150 mm was type b), i.e. interlaminar failure at the fiber-matrix interface (MF). Out of ten specimens with ℓ =175 mm, four specimens failed as the peak load was reached while six specimens presented a drop in the load response when the peak was reached, followed by a nominally constant load portion (plateau) until failure. The load responses of specimens with long bonded length ($\ell \geq$ 200 mm) had generally three different behaviors depending on the failure mode. Out of fifty-one specimens with $\ell \geq$ 200 mm, twenty-six specimens presented a drop after the peak was reached followed by an approximatively constant load branch (plateau). For these specimens, which failed at the matrix-fiber interface (MF), the load-carrying capacity or plateau load, P_{crit}, was evaluated as the average value of the applied load in the range of global slips $[g_1,g_2]$. The value g_1 was defined as the value of global slip that corresponded to the first substantial drop in the load response after the peak was reached. If the drop was

not clearly identifiable in the response, the first valley after the peak was used to determined g_1 (as in the case of Figure 5c). Whereas, the value g_2 was defined as the last value of global slip that preceded the failure of the specimen (Figure 5c). For all specimens that presented a constant plateau in the load response, i.e. the aforementioned twenty-six specimens with $\ell \geq 200$ mm and the six specimens with a bonded length equal to 175 mm, the values of g_1, g_2 and P_{crit} are reported in Table 3. These specimens are referred to as "Plateau specimens" in the remainder of the paper. In addition, for these specimens, the average value of LVDT c ($\overline{w_c}$) and LVDT d ($\overline{w_d}$) in the range [g_1,g_2] was reported in Table 3. The maximum value of $\overline{w_c}$ and $\overline{w_d}$ resulted equal to 2.80 mm and 2.99 mm, respectively, which supports the choice of arranging the masonry block 1 mm forward with respect to the initial alignment (see Section 2.3). The same displacement measured for similar tests with SRP-concrete joints [54] was lower than 1 mm due to the absence of the mortar joints. Generally, the longer is the bonded length the longer is the plateau [43]. Six specimens with $\ell \geq 200$ mm failed because of the rupture of the fibers (FR) and the load increased until failure. Nineteen specimens with $\ell \geq 200$ mm showed a type b) failure mode (MF) with an always increasing load response or with a load response characterized by large drops without a constant plateau. In Figure 5d, the load responses for specimens DS_345_50_LD_LM_3, DS_345_50_LD_LM_5, and DS_345_50_LD_LM_10 are reported.

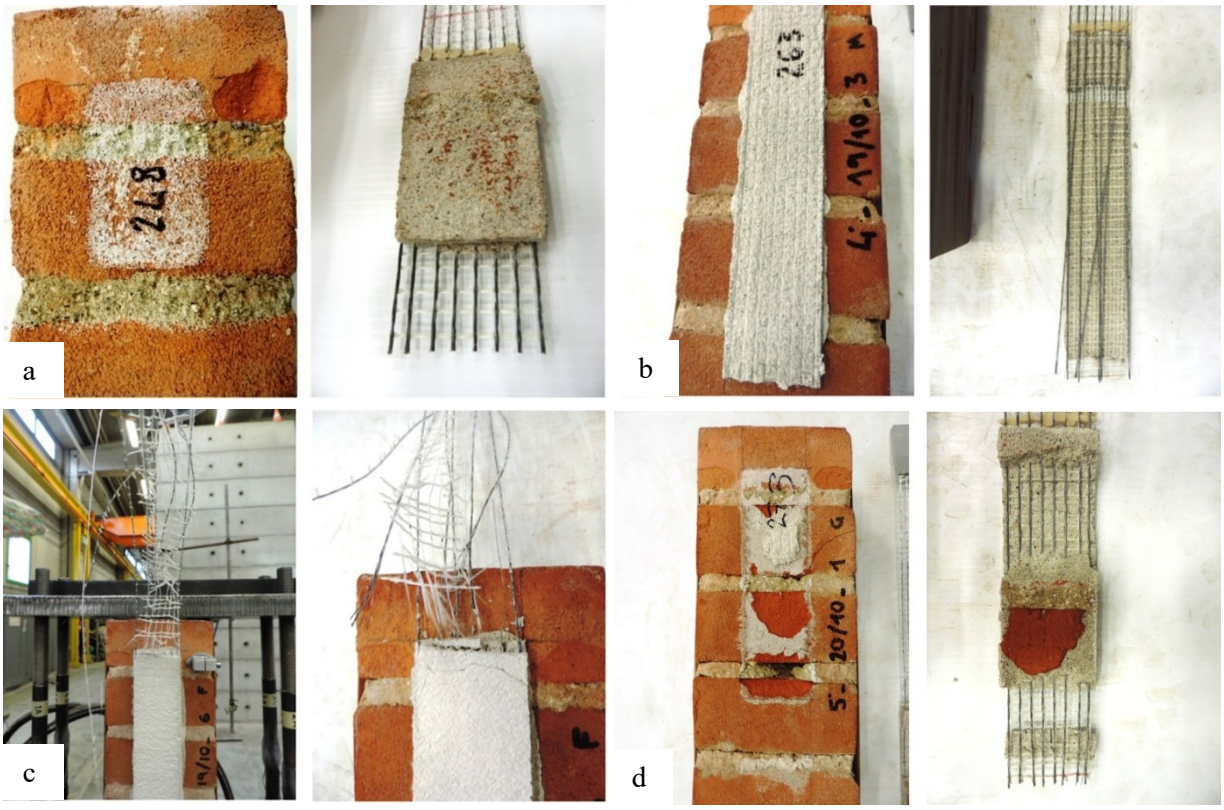

Figure 6. Failure modes: a) debonding at the matrix-masonry interface (MM), b) interlaminar failure at the matrix-fiber interface (MF), c) rupture of the fibers (FR), d) mixed failure mode (SF/MF).

It can be observed that the load responses had a similar trend until approximatively 8 kN. After 8 kN, interlaminar failure started in specimen DS_345_50_LD_LM_3 and the cohesive crack at the matrix-fiber interface continued to propagate gradually until failure, which resulted in the presence of a plateau in the response. Specimen DS_345_50_LD_LM_5 had a behavior similar to specimen DS_345_50_LD_LM_10 until approximatively 12 kN, after which the interlaminar failure quickly propagated (MF) with sudden drops in the load response. Specimen DS_345_50_LD_LM_10 showed a monotonic load response until the rupture of the fibers. Only the value of the peak load, P^*, was reported in Table 3 for all the specimens for which load response didn't show a plateau. The plots of Figure 5d is symptomatic of how the variability of the mortar properties and the impregnation of the fibers could entail for a switch among the different failure modes and, as a consequence, among the different load responses.

4. Discussion of results

A large scatter in the experimental results can be observed in Table 3 and Figure 7. Figure 7a shows all the responses corresponding to $\ell \geq 175$ mm. Figure 7b includes only the response of those specimens with $\ell \geq 175$ mm that exhibited a plateau.

Considering specimens DS_315_50_LD_LM_B2_2 and DS_315_50_LD_LM_B2_3, which were cast using the same batch of matrix mortar (B2) and using the same bonded length equal to 315 mm, the peak load, P^*, was equal to 12.75 kN and 6.21 kN, respectively. The different response can be partially ascribed to different saturation levels of the masonry blocks prior to applying the SRG strip. It is possible that if the masonry block was not fully soaked, it absorbed part of the water of the matrix mortar during and after the application of the composite strip, which caused a reduction of the matrix mortar mechanical properties that translated into low bond properties. In addition, as reported in Table 3, it can be observed that both the compressive and fracture properties of the mortar were quite scattered among the different batches. Batch B3 had a compressive strength equal to 15.7 MPa that was 39% higher than the compressive strength of batch B4, and a fracture energy equal to 30 N/m that was similar to the value found for batch B4. The scatter of the matrix mortar properties among different batches contributed to the scatter of the single-lap shear test results. A third reason for the scatter in the experimental results is related to the application of the SRG composite to the masonry substrate, since for all specimens it was difficult to control that the matrix mortar was fully penetrating through and impregnating each steel fiber during casting of SRG strips.

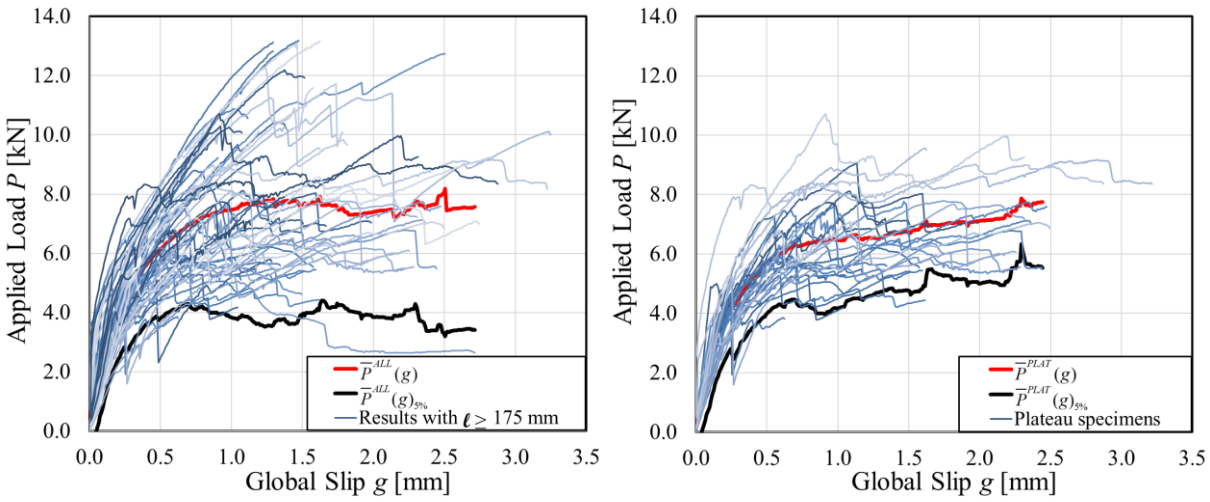

a b

Figure 7. Experimental load responses: a) all load responses with $\ell \geq 175$ mm and corresponding average response $\overline{P}^{ALL}(g)$; b) all Plateau specimen responses with $\ell \geq 175$ mm and corresponding average response $\overline{P}^{PLAT}(g)$.

Figure 8a reports the average peak load and the average plateau load for different bonded lengths. The joint capacity response shown in Figure 8a is referred to as $P_{crit}(\ell)$ in the remainder of the paper. The average of the peak load is represented with a blue circular marker in Figure 8a for $\ell \leq 175$ mm, while the average of the plateau load is represented with a red triangular marker for $\ell > 175$ mm. The average of the plateau load for specimens with $\ell = 280$ mm was omitted because it was possible to evaluate P_{crit} only for specimen DS_280_50_LD_LM_4, which cannot be considered statistically relevant. The choice of plotting the peak load for specimens with short bonded lengths was determined by the fact that for these specimens the test failed prior to observing a plateau in the load response. Figure 8a shows an increase of the average of the peak load with the bonded length when $\ell \leq 175$ mm, then the average of the plateau load has an approximatively constant trend between $\ell = 175$ mm and $\ell = 315$ mm, with values that range from 4.95 kN to 6.22 kN. The maximum value of the average plateau load is observed for $\ell = 345$ mm and results equal to 7.91 kN. Due to the trend observed in Figure 8a, it can be stated that, for the SRG

composite studied in this experimental work, the effective bond length L_{eff}, i.e. the length of the composite strip needed to fully establish the stress transfer between the composite strip and the substrate, is between 175 mm and 200 mm. This fact is confirmed from the load responses analyzed in Section 3, that feature a constant plateau when $\ell \geq 175$ mm. In this Section, the evaluation of the effective bond length didn't take into account those specimens (twenty-five out of the seventy-eight) with $\ell \geq 200$ mm that didn't show a constant plateau in the load response. They usually reached the rupture of the fibers or values of the peak load close to the value associated with the rupture of the fibers. The authors chose to neglect these specimens for the determination of the effective bond length since they were not representative of the actual interlaminar debonding phenomenon and thus can entail for misleading results. For the sake of completeness, Figure 8b shows the average value of the peak load for different bonded lengths, considering all specimens tested at the standard rate (0.00084 mm/s). The joint capacity response shown in Figure 8b is referred to as $P^*(\ell)$ in the remainder of the paper. It could be noted that, given the bonded length, values of the $P^*(\ell)$ of Figure 8b are in general higher than the $P_{crit}(\ell)$ ones, since the former includes also specimens that didn't show a constant plateau in the load response, i.e. specimens that failed reaching a load equal to or close to the one corresponding to the rupture of the fibers.

Figure 8c shows a comparison between direct single-lap shear tests performed using two different test rates and a constant bonded length equal to 315 mm. The grey area represents the envelope of the experimental tests performed at the standard rate (0.00084 mm/s), while the black dashed line is the average response of those tests, which is obtained by averaging the values of P for each value of g. Similarly, the red area represents the envelope of the experimental tests performed at a rate (0.0084 mm/s) that was ten times the standard one. In addition, the load responses of the three specimens tested at a higher rate are reported for the sake of clarity. A plateau can be observed also for these three specimens. The average peak load for specimens tested at standard rate and ten times the standard rate resulted equal to 7.57 kN and 10.41 kN, respectively. It appears that this type of composites exhibits a rate effect [55], as shown in Figure 8c. The average curve of specimens tested at a rate equal to 0.0084 mm/s is above the

average curve of specimens tested at standard rate. On the other hand, it should be pointed out that only three specimens were tested with a higher rate and therefore more results are needed to confirm this trend.

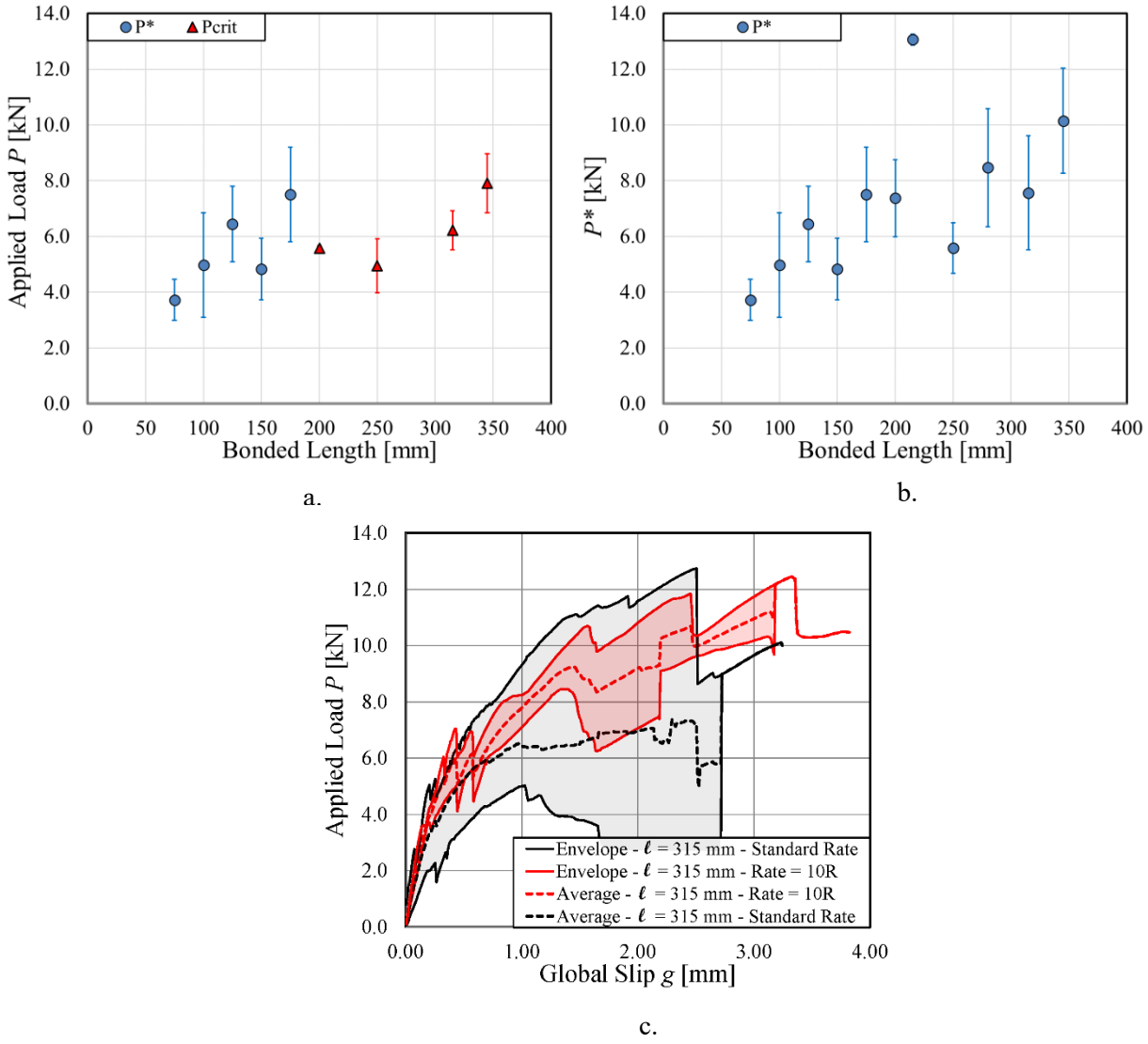

Figure 8. a) $P_{crit}(\ell)$ response; b) $P^*(\ell)$ response; c) Load-global slip envelope for specimens with $\boldsymbol{\ell}$ =315 mm and two different rates (0.00084 mm/s and 0.0084 mm/s).

5. Indirect calibration of the cohesive material law

In this Section, the cohesive material law (CML) that characterizes the bond behavior of the SRG-masonry joints tested in this experimental work will be calibrated through two different indirect methods. The CML will be referred to as τ(*s*) relationship in this work. As described in Section 3, the debonding process of SRG-masonry joints mainly occurs at the matrix-fiber interface. Thus, the slip *s* in the τ(*s*) relationship is the relative displacement of the steel fibers with respect to the layer of the matrix bonded to the substrate (considered as perfectly bonded) and τ is the shear stress at the matrix-fiber interface. It should be pointed out that as a result of the calibration the CML obtained should be representative of the interlaminar failure mode MF. Nevertheless, as the results of an experimental campaign could be limited or the failure modes not clearly identified, this paper presents the calibration process considering either the entire set of data or only those specimens that exhibited an interlaminar failure mode.

Once the τ (*s*) relationship is assigned, it is possible to: i) derive the maximum load as a function of the bonded length $P_{\max}(\ell)$ and ii) compute the *P*(*g*) response associated with a given $\boldsymbol{\ell}$ [44]. The first indirect method calibrates the CML using the peak or the debonding load versus bonded length responses (experimental joint capacity responses $P^{*}(\ell)$ or $P_{crit}(\ell)$, respectively). The second indirect method calibrates the CML using two average load-global slip responses obtained by either considering all the specimens with $\boldsymbol{\ell} \geq 175$ mm (Figure 7a) or only those specimens with $\boldsymbol{\ell} \geq 175$ mm that exhibit a plateau (Figure 7b).

It should be noted that a CML for the matrix-substrate interface cannot be obtained as only few specimens exhibited crack propagation at this interface and they were typically characterized by $\boldsymbol{\ell} \leq 100$ mm.

5.1 Functions adopted for the definition of the cohesive material law

Both calibration methods require the adoption of an analytical expression of the CML whose parameters are determined by fitting the experimental data. Two different analytical expressions of the CML will be used in this study. The first CML is derived from the expression proposed by Dai et al. [56]:

$$\tau(s) = \mathrm{A}\left(e^{-\alpha s} - e^{-2\alpha s}\right) \tag{1}$$

where $\boldsymbol{p}$ = [A, α] is the set of unknown parameters. Eq. (1) implies that the maximum value of the slip, s_f, beyond which no shear stress transfer occurs approaches infinity (i.e. $s_f \to +\infty$). Eq. (1) represents a cohesive material law characterized by shear stress equal to zero when s = 0 (τ(0)=0).

The second CML is a tri-linear function, proposed by Focacci and Carloni [57]:

$$\tau(s) = \begin{cases} \tau_0 + \dfrac{\tau_m - \tau_0}{s_m} s & \text{if} \quad 0 \le s \le s_m \\ \tau_{01} - \dfrac{\tau_{01}}{s_{01}} s & \text{if} \quad s_m \le s \le s_c \\ \tau_{02} - \dfrac{\tau_{02}}{s_f} s & \text{if} \quad s_c \le s \le s_f \end{cases} \tag{2}$$

where $\boldsymbol{p}$ =[τ_0, τ_{01}, τ_{02}, τ_m, s_{01}, s_f, s_m] is the set of unknown parameters. The CML defined by Eq. (2) is characterized by shear stress equal to τ_0 when s = 0. Eq. (1) implies an infinite effective bond length while Eq. (2) implies a finite effective bond length, as discussed in [57] and [58].

5.2 Indirect calibration from the $P_{crit}(\ell)$ and $P^*(\ell)$ responses

The first method for the indirect calibration of the CML was proposed by Focacci et al. [44] and is employed in the present work to fit the experimental load versus bonded length responses $P_{crit}(\ell)$ and $P^*(\ell)$, shown in Figure 8a-b, with the function $P_{\max}(\ell)$ associated with the assigned CML. For the sake of brevity, the procedure of the indirect calibration of the CML that uses the $P_{crit}(\ell)$ response is referred to as $CAL_{Pcrit(\ell)}$ while the procedure of the indirect calibration that employs the $P^*(\ell)$ response is referred

to as $CAL_{P*(\ell)}$. The analytical evaluation of the $P_{\max}(\ell)$ associated with an assigned $\tau(s)$ is based on the following differential equation [44]:

$$\frac{\mathrm{d}^2 s}{\mathrm{d}y^2} = \frac{b_f}{E_f A_f}\tau(s) \tag{3}$$

where $s = s(y)$ is the slip at location y, referred to the y-axis shown in Figure 1. It should be noted that the origin of the y-axis is the free end, i.e. the end of the bonded region. The area of the fiber sheet can be evaluated as $A_f = b_f t^*_{f,\mathrm{LD}}$. Employing Eq. (3), the analytical load response $P(g)$ was determined for each bonded length $\boldsymbol{\ell}$ with the procedure described in [44]. The analytical $P_{\max}(\boldsymbol{\ell})$ response was then obtained by associating to each bonded length $\boldsymbol{\ell}$ the maximum load $P_{\max}$ of the load response $P(g)$ relative to the bonded length $\boldsymbol{\ell}$ itself. The unknown parameters $\boldsymbol{p}$ are determined by minimizing the distance between the analytical $P_{\max}(\boldsymbol{\ell})$ and the experimental joint capacity response $P^*(\ell)$ (Fig. 15b) in the case of the $CAL_{P*(\ell)}$ calibration and the experimental joint capacity response $P_{crit}(\ell)$ (Fig. 15a) in the case of the $CAL_{Pcrit(\ell)}$ calibration.

It has been observed in Section 3 that specimens with $\boldsymbol{\ell}$ shorter than 125 mm had a failure mode characterized by the detachment of the SRG strip from the masonry substrate (MM). All the remaining specimens considered in the best fit procedure had a failure mode characterized by interlaminar failure at matrix-fiber interface (MF). Thus, specimens with $\boldsymbol{\ell}$ equal to 75 mm and 100 mm, should not be considered for the fitting, since the cohesive material law that governs the fracture process is different with respect to the other specimens. The authors decided to include these specimens in the best fit procedure. Because of the hierarchy of interface failures, it is possible that the interlaminar failure for short bonded lengths cannot be obtained experimentally. Thus, this would mean that this type of failure would require a higher load than the MM failure for short bonded lengths. Keeping this mind, the authors

used all lengths to determine the CML through the best fit procedure, although it might not be fully representative of specimens with $\ell \leq 100$ mm.

5.3 Indirect calibration from the load-global slip response

The second method for the indirect calibration of the CML employs the load-global slip responses. Each load-global slip response plotted in Figure 7 can be used separately to calibrate the CML, which would result in a set of CMLs calibrated against the single load responses. However, in this study the average experimental responses obtained from Figure 7a and 7b are considered. The average experimental load response is obtained by averaging the loads of the $P(g)$ responses of the specimens for each value of g. The average experimental response is evaluated considering two different sets of data. The average experimental response referred to as $\overline{P}^{ALL}(g)$ is determined considering all the load-global slip responses of specimens with $\ell \geq 175$ mm (Figure 7a); while the average experimental response referred to as $\overline{P}^{PLAT}(g)$ is determined considering the load-global slip responses of the "Plateau specimens" (see Section 3 and Figure 7b), i.e. the specimens that feature a plateau (P_{crit}) and therefore characterized by an interlaminar failure mode at the matrix-fiber interface (MF).

The evaluation of the average load was not performed for values of g for which less than 6 values of the load were available. Thus, the $\overline{P}^{ALL}(g)$ and the $\overline{P}^{PLAT}(g)$ curves are cropped at that value of g. The average load-global slip response $\overline{P}^{ALL}(g)$ is reported in Figure 7a; while the average load-global slip response $\overline{P}^{PLAT}(g)$ is reported in Figure 7b. In addition, the 5th percentile of the $\overline{P}^{ALL}(g)$ response ($\overline{P}^{ALL}(g)_{5\%}$) and the 5th percentile of the $\overline{P}^{PLAT}(g)$ response ($\overline{P}^{PLAT}(g)_{5\%}$) are reported in Figure 7a-b, respectively. For both sets of data considered, the evaluation of the 5th percentile of the average experimental load-global slip response was evaluated using the following equations:

$$\overline{P}^{ALL}(g)_{5\%} = \overline{P}^{ALL}(g) - 1.645\sigma^{ALL}(g) \tag{4}$$

$$\overline{P}^{PLAT}(g)_{5\%} = \overline{P}^{PLAT}(g) - 1.645\sigma^{PLAT}(g) \tag{5}$$

where $\sigma^{ALL}(g)$ and $\sigma^{PLAT}(g)$ are the corresponding standard deviations referred to $\overline{P}^{ALL}(g)$ and $\overline{P}^{PLAT}(g)$, respectively, for any value of *g*.

Averaging of experimental load responses associated with different bonded lengths is justified because the analytical *P*(*g*) response associated with a given bonded length, ℓ_1, coincides with the *P*(*g*) response of a shorter bonded length, ℓ_2, up to the point $(\overline{g}, P_2)$, defined as:

$$\begin{aligned} &\overline{g} = s(\ell_2) \\ &P_2 = E_f A_f \left.\frac{\mathrm{d}s}{\mathrm{d}y}\right|_{y=\ell_2} \end{aligned} \tag{6a,b}$$

when *s*(*y*) is the solution of Eq. (3) with *s*=0 only at *y*=0 (free end), i.e. when the stress transfer occurs for the entire bonded length ℓ_2.

Once the CML is chosen (see Section 5.1), the analytical *P*(*g*) response corresponding to a bonded length equal to 345 mm, $P(g)_{\ell=345}$, is evaluated through the procedure described in [44] and based on Eq. (3). The bonded length is chosen to be the greatest value of the experimental data because the analytical response $P(g)_{\ell=345}$ overlaps with the responses associated with shorter bonded lengths. The CML is then calibrated using the least square method to minimize the distance between the analytical $P(g)_{\ell=345}$ response and the average experimental responses $\overline{P}^{ALL}(g)$ or $\overline{P}^{PLAT}(g)$, which will allow to determine the set of parameters $\boldsymbol{p}$ of the CML. The procedure of the indirect calibration that employs the $\overline{P}^{ALL}(g)$

response is referred to as $CAL_{PALL(g)}$; while the procedure of the indirect calibration based on the $\overline{P}^{PLAT}(g)$ response is referred to as $CAL_{PPLAT(g)}$.

5.4 Results of the indirect calibration of the CML

In this Section, the results of the indirect calibration of the CML described in Sections 5.2 and 5.3 are presented through Figure 9 and Figure 10. Figure 9a shows a comparison between the CML calibrated through different joint capacity responses using both the tri-linear [57] and Dai et al. [56] functions. From Figure 9a it can be observed that the CML obtained from $CAL_{P*(\ell)}$ reaches greater values of s_f than the CML obtained from $CAL_{Pcrit(\ell)}$. This fact can be explained by considering that the experimental joint capacity $P^*(\ell)$ does not show a constant trend as the bonded length increases (Figure 8b, Figure 10a), which is on the other hand observed for the joint capacity $P_{crit}(\ell)$ (Figure 8a, Figure 10b). Figure 9a shows that the maximum shear stress τ_{max} obtained through $CAL_{P*(\ell)}$ is similar to the one obtained through $CAL_{Pcrit(\ell)}$, if the same function is employed.

Figure 9b indicates that the tri-linear [57] and Dai et al. [56] CMLs obtained from $CAL_{Pcrit(\ell)}$ and $CAL_{PPLAT(g)}$ are similar. This observation suggests that if the plateau load is considered, the method selected to calibrate the CML is not crucial to obtain the fracture properties of the interface.

The CMLs obtained from $CAL_{P*(\ell)}$ and $CAL_{PALL(g)}$, shown in Figure 9c, are somewhat different. This fact is somehow related to what observed before. In other words, if the goal of the calibration process is to obtain a CML representative of the interlaminar failure mode, then the influence of the load responses corresponding to the failure of the fibers (failure more FR) is more pronounced on the joint capacity $P^*(\ell)$ rather than on the average load response $\overline{P}^{ALL}(g)$.

The CMLs obtained from $CAL_{PALL(g)}$ compare well with the CMLs obtained from $CAL_{PPLAT(g)}$ (Figure 9d). This is partially connected to the fact (see comment about Figure 9c) that when the applied load-global slip response $P(g)$ is used to calibrate the CML the effect of the scatter of the peak loads on the average $P(g)$ curve is not as critical as for the joint capacity $P(\ell)$.

Overall, it should be noted that the values of the maximum shear stress τ_{max} are roughly comprised between 1.0 MPa and 1.5 MPa, while the values of the slip corresponding to the complete debonding are consistent with the values of g_1 reported in Table 3.

Figure 10c-d compare the experimental $P(g)$ responses and the analytical $P(g)$ responses obtained from the indirect calibrations. As expected, the best match is obtained when the analytical response is obtained through best fitting of the corresponding experimental response. For example, the analytical $P(g)$ curve obtained from $CAL_{P*(\ell)}$ employing both CML functions does not agree well with the experimental $\overline{P}^{ALL}(g)$ curve (Figure 10c). On the other hand, independently of the CML chosen, the analytical $P(g)$ curve obtained from $CAL_{PALL(g)}$ agrees very well with the experimental $\overline{P}^{ALL}(g)$ curve.

In Figure 10a-b a comparison between the experimental $P(\ell)$ responses ($P^*(\ell)$ and $P_{crit}(\ell)$) and the analytical $P(\ell)$ responses ($P_{max}(\ell)$) obtained from the indirect calibrations is made. Similarly to what observed for Figure 10c-d, the best match between the response obtained from the calibration and the experimental one occurs when the calibration is made against the same experimental curve used to compare the results. The shape of the CML function does not influence this match.

Table 4 summarizes the most important fracture mechanics parameters obtained from the indirect calibrations. Lower values of the fracture energy, i.e. the area under the CML curve, are obtained with $CAL_{Pcrit(\ell)}$ and $CAL_{PPLAT(g)}$, which employ the experimental responses of those specimens that exhibit the interlaminar failure. The values of the fracture energy are consistent between the calibrations that employ two different CML functions. The values of the effective bond length, L_{eff}, which represents the minimum

length to fully establish the stress transfer, are very similar among the different calibrations when the tri-linear [57] CML is employed.

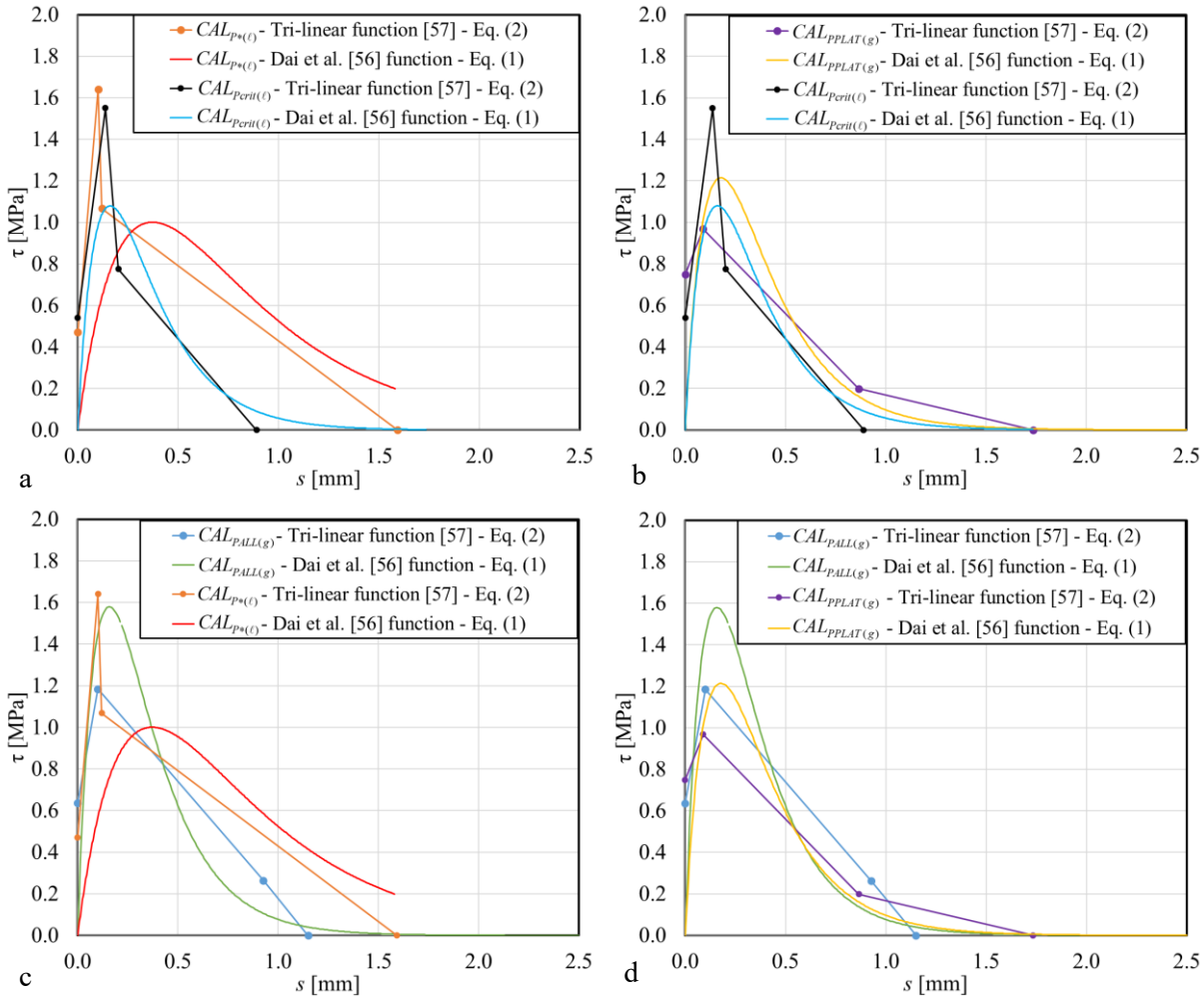

Figure 9. Cohesive material laws (CML) obtained from the indirect calibrations: a) comparison between the CMLs obtained from $CAL_{P*(\ell)}$ and $CAL_{Pcrit(\ell)}$; b) comparison between the CMLs obtained from $CAL_{Pcrit(\ell)}$ and $CAL_{PPLAT(g)}$; c) comparison between the CMLs obtained from $CAL_{P*(\ell)}$ and $CAL_{PALL(g)}$; d) comparison between the CMLs obtained from $CAL_{PALL(g)}$ and $CAL_{PPLAT(g)}$.

A similar comment can be made for Dai et al. function [56], when specimens that exhibit a plateau load, i.e. interlaminar failure, are used. It should be noted that for the Dai et al. [56] CML, an arbitrary criterion for

the effective bond length should be established [54]. The authors used as the effective bond length, the length needed to transfer 96% of the bond capacity as suggested in [56]. It can be observed that the effective bond length L_{eff}, determined through the indirect calibration of the CML is similar to the value obtained from the analysis of the experimental tests, presented in Section 4. Finally, the values of the slip s_m, which corresponds to the maximum shear stress, are quite consistent among the different calibrations for each CML function.

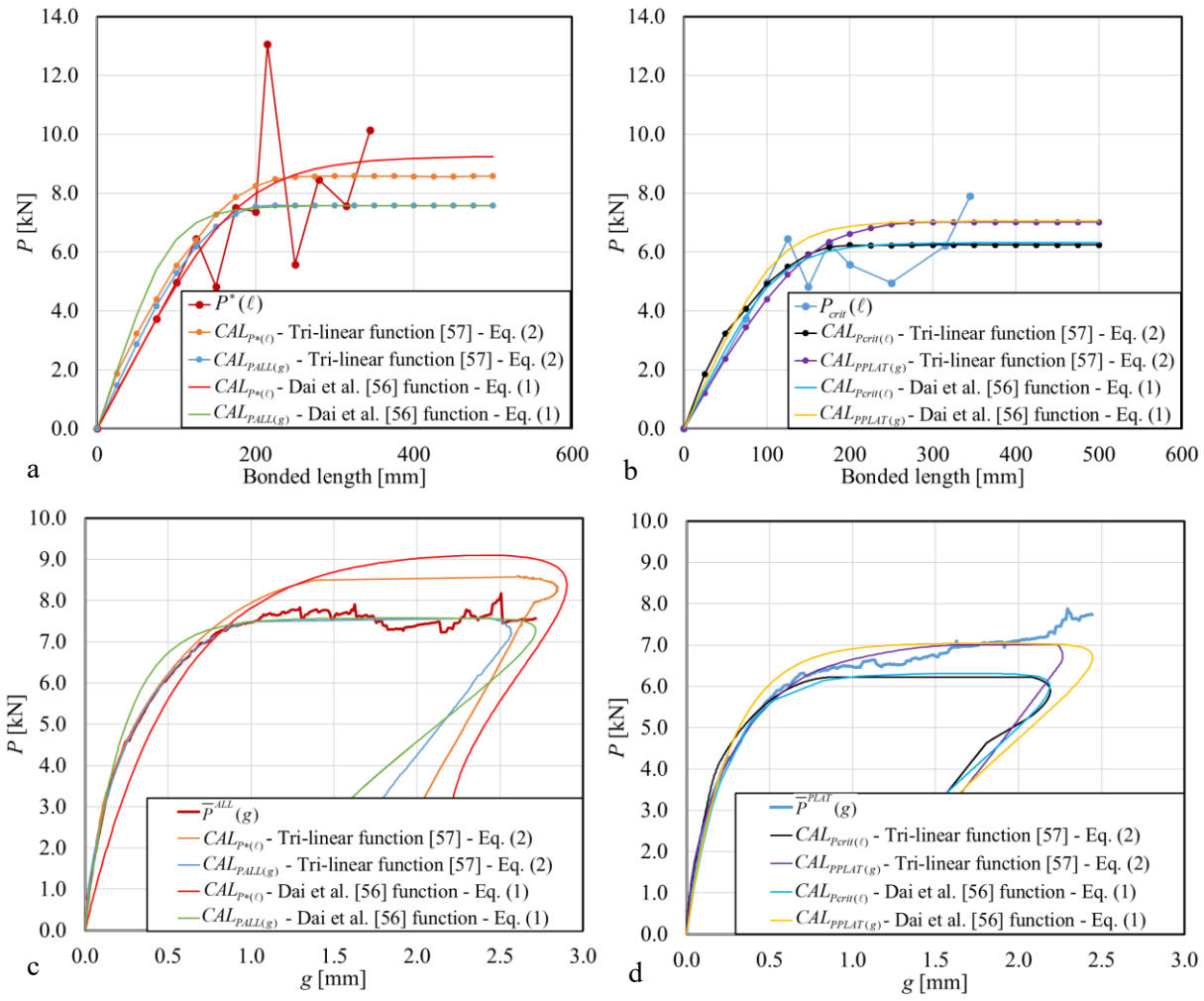

Figure 10. Comparison of the analytical joint capacities and load responses obtained from the parameters of the indirect calibration with the corresponding experimental curves: a) $P^*(\ell)$ vs. $P_{max}(\ell)$

from $CAL_{P*(\ell)}$ and $CAL_{PALL(g)}$; b) $P_{crit}(\ell)$ vs. $P_{\max}(\ell)$ from $CAL_{Pcrit(\ell)}$ and $CAL_{PPLAT(g)}$; c) $\overline{P}^{ALL}(g)$ vs. $P(g)$ from $CAL_{P*(\ell)}$ and $CAL_{PALL(g)}$; d) $\overline{P}^{PLAT}(g)$ vs. $P(g)$ from $CAL_{Pcrit(\ell)}$ and $CAL_{PPLAT(g)}$.

Table 4. Fracture parameters obtained from the indirect calibrations.

Calibration	Tri-linear function [57] – Eq. (2)				Dai et al. [56] function – Eq. (1)			
	G_F [N/m]	L_{eff} [mm]	τ_{max} [MPa]	s_m [mm]	G_F [N/m]	L_{eff} [mm]	τ_{max} [MPa]	s_m [mm]
$CAL_{Pcrit(\ell)}$	485	217	1.55	0.14	500	226	1.08	0.16
$CAL_{P*(\ell)}$	918	267	1.64	0.10	964	381	1.00	0.37
$CAL_{PALL(g)}$	719	209	1.19	0.10	719	191	1.58	0.16
$CAL_{PPLAT(g)}$	616	287	0.97	0.09	623	224	1.21	0.18

6. Conclusions

In this paper, an extensive experimental work was presented. Single-lap shear tests were performed to study the bond behavior between steel reinforced grout (SRG) strips and a masonry substrate, which is the most critical aspect for strengthening applications. The experimental results were quite scattered, which is related to the variability of the hydraulic mortar employed and its ability to impregnate the fibers. Different failure modes were observed: a) at the matrix-masonry interface (MM), b) interlaminar failure at the matrix-fiber interface (MF), c) rupture of the steel fibers (FR), and d) mixed failure mode (SF/MF) characterized by the detachment of the SRG strip from the substrate with a thin layer of masonry attached to it (SF) in a limited portion of the bonded region and by the interlaminar failure (MF) in the remaining portions of the bonded region. For SRGs, debonding typically occurs at the fiber-matrix interface, i.e. interlaminar failure. The overarching goal of this work was the determination of the constitutive law of the interface, which is typically referred to as cohesive material law (CML), for the case of interlamianr

failure. Since direct measurements of the strain on the fibers are hindered by the external layer of matrix, two indirect calibration methods to obtain the CML were employed. The first method used the experimental peak or the plateau load versus bonded length responses ($P^*(\ell)$ or $P_{crit}(\ell)$, respectively); whereas, the second method used two average load-global slip responses obtained by either considering all specimens or only those that exhibited an interlaminar failure mode, which is associated with a plateau in the response. The reason behind the use of two set of data, which either include or exclude those specimens that exhibited the rupture of the fibers, is to understand the sensitivity of the calibration procedure on the number of tests and scatter of the results. In fact, if only few tests are performed and the failure modes are different one could have no choice but include all data and would need to understand if the CML obtained is representative of the bond behavior.

Overall, the two calibration methods applied to two different sets of data provide similar CMLs. Therefore, when a limited number of tests is available, the inclusion of all data might not compromise the description of the interfacial behavior. However, it was noted that the two calibration methods provide similar and consistent results when used with the set of data that include only specimens with interlaminar failure. On the other hand, when all specimens are included, the CMLs from the two methods are somewhat different one another and with respect to the ones with fewer specimens. In addition, the values of the fracture energy, i.e. the area under the CML curve, obtained when the entire set of data is used is greater than the value of the fracture energy obtained from the subset of data that is associated with interlaminar failure.

Acknowledgments

Technicians of the laboratory LISG (Laboratory of Structural and Geotechnical Engineering) at University of Bologna are gratefully acknowledged. Kerakoll S.p.A. of Sassuolo, Italy, is gratefully acknowledged for providing the composite materials. Financial support by the Italian Ministry of Education, Universities and Research MIUR is gratefully acknowledged (PRIN2015 “Advanced

mechanical modeling of new materials and structures for the solution of 2020 Horizon challenges" prot. 2015JW9NJT_018).

References

[1] P. Foraboschi, "Strengthening of masonry arches with fiber-reinforced polymer strips," *Journal of composites for construction,* vol. 8(3), pp. 191-202, 2004.

[2] L. Rovero, F. Focacci and G. Stipo, "Structural behavior of arch models strengthened using fiber-reinforced polymer strips of different lengths," *Journal of Composites for Construction,* vol. 17(2), pp. 249-258, 2012.

[3] P. Foraboschi, "Effectiveness of novel methods to increase the FRP-masonry bond capacity," *Composites Part B: Engineering,* vol. 107, pp. 214-232, 2016.

[4] C. Carloni and K. V. Subramaniam, "Investigation of the interface fracture during debonding between FRP and masonry," *Advances in Structural Engineering,* vol. 12(5), pp. 731-743, 2009.

[5] C. Carloni and K. V. Subramaniam, "FRP-masonry debonding: numerical and experimental study of the role of mortar joints," *Journal of Composites for Construction,* vol. 16(5), pp. 581-589, 2012.

[6] C. Mazzotti, B. Ferracuti and A. Bellini, "Experimental bond tests on masonry panels strengthening by FRP," in *Proceedings of 6th international conference on FRP composites in civil engineering (CICE 2012)*, Rome, 2012.

[7] P. Carrara, D. Ferretti and F. Freddi, "Debonding behavior of ancient masonry elements strengthened with CFRP sheets," *Composites Part B: Engineering,* vol. 45(1), pp. 800-810, 2013.

[8] S. Briccoli Bati, M. Fagone and G. Ranocchiai, “The effects of mortar joints on the efficiency of anchored CFRP sheets reinforcements of brick-masonry,” *Key Engineering Materials,* vol. 624, pp. 575-583, 2015.

[9] F. Ceroni, A. Garofano, M. Pecce and G. M. Procaccini, “Effect of the presence of mortar joints in the bond behaviour of tuff masonry elements,” *Key Engineering Materials,* vol. 624, pp. 526-533, 2015.

[10] M. Panizza, E. Garbin, M. R. Valluzzi and C. Modena, “Experimental study of the bond of FRP applied to natural stones and masonry prisms,” *Key Engineering Materials,* vol. 624, pp. 453-460, 2015.

[11] C. Mazzotti, E. Sassoni, A. Bellini, B. Ferracuti and E. Franzoni, “Strengthening of masonry elements by FRP: Influence of brick mechanical and microstructural properties,” *Key Engineering Materials,* vol. 624, pp. 330-337, 2014.

[12] B. Mobasher and Y. L. Cheng, “Mechanical properties of hybrid cement-based composites,” *ACI Materials Journal,* vol. 93, pp. 284-292, 1996.

[13] T. Bischoff, B. Wulfhorst, G. Franzke, P. Offermann, A. M. Bartl, H. Fuchs, R. Hempel, M. Curbach, U. Pachow and W. Weiser, “Textile reinforced concrete fac¸ade elements - An investigation to optimize concrete composite technologies,” *Proceedings of the 43rd International SAMPE Symposium,* pp. 1790-1802, 1998.

[14] M. Curbach and F. Jesse, “High-performance textile-reinforced concrete,” *Structural engineering international,* vol. 9(4), pp. 289-291, 1999.

[15] M. Curbach and R. Ortlepp, “Besonderheiten des verbundverhaltens von verstaerkungsschichten aus textilbewehrtem,” *Proceedings of the 2 nd colloquium on textile reinforced structures, Dresden, Germany, September 2003,* pp. 361-374.

[16] M. Curbach and A. Brueckner, “Textile strukturen zur querkraftverstaerkung von stahlbetonbauteilen,” *Proceedings of the 2nd colloquium on textile reinforced structures. Dresden, Germany, September 2003,* pp. 347-360.

[17] A. Brückner, R. Ortlepp and M. Curbach, “Textile reinforced concrete for strengthening in bending and shear,” *Materials and structures,* vol. 39(8), pp. 741-748, 2006.

[18] A. D'Ambrisi and F. Focacci, “Flexural strengthening of RC beams with cement-based composites,” *Journal of Composites for Construction,* vol. 15(5), pp. 707-720, 2011.

[19] C. Escrig, L. Gil and E. Bernat-Maso, "Experimental comparison of reinforced concrete beams strengthened against bending with different types of cementitious-matrix composite materials," *Construction and Building Materials,* vol. 137, pp. 317-329, 2017.

[20] T. C. Triantafillou, C. G. Papanicolau, P. Zissimopoulos and T. Laourdekis, “Concrete confinement with textile-reinforced mortar jackets,” *ACI structural journal,* vol. 103(1), pp. 28-37, 2006.

[21] T. D'Antino, L. H. Sneed, C. Carloni and C. Pellegrino, “Bond behavior of the FRCM-concrete interface,” in *Proceedings of the 11th international symposium*, Guimaraes, 2013.

[22] V. Alecci, F. Focacci, L. Rovero, G. Stipo and M. De Stefano, "Extrados strengthening of brick masonry arches with PBO–FRCM composites: Experimental and analytical investigations," *Composite Structures,* vol. 149, pp. 184-196, 2016.

[23] V. Alecci, F. Focacci, L. Rovero, G. Stipo and M. De Stefano, “Intrados strengthening of brick masonry arches with different FRCM composites: experimental and analytical investigations,” *Composite Structures,* vol. 176, pp. 898-909, 2017.

[24] A. Borri, P. Casadei, G. Castori and J. Hammond, "Strengthening of brick masonry arches with externally bonded steel reinforced composites," *Journal of composites for construction,* vol. 13(6), pp. 468-475, 2009.

[25] L. Garmendia, J. T. San-José, D. García and P. Larrinaga, “Rehabilitation of masonry arches with compatible advanced composite material,” *Construction and Building Materials,* vol. 25(12), pp. 4374-4385, 2011.

[26] V. Giamundo, G. P. Lignola, G. Maddaloni, A. Balsamo, A. Prota and G. Manfredi, “Experimental investigation of the seismic performances of IMG reinforcement on curved masonry elements,” *Composites Part B: Engineering,* vol. 70, pp. 53-63, 2015.

[27] L. Garmendia, I. Marcos, E. Garbin and M. R. Valluzzi, “Strengthening of masonry arches with textile-reinforced mortar: experimental behaviour and analytical approaches,” *Materials and structures,* vol. 47(12), pp. 2067-2080, 2014.

[28] C. Carloni, C. Mazzotti, M. Savoia and K. V. Subramaniam, “Confinement of Masonry Columns with PBO FRCM Composites,” *Key Engineering Materials,* vol. 624, pp. 644-651, 2014.

[29] A. Bellini, A. Incerti, M. Bovo and C. Mazzotti, “Effectiveness of FRCM Reinforcement Applied to Masonry Walls Subject to Axial Force and Out-Of-Plane Loads Evaluated by Experimental and Numerical Studies,” *International Journal of Architectural Heritage,* vol. 12(3), pp. 376-394, 2018.

[30] F. G. Carozzi and C. Poggi, “Mechanical properties and debonding strength of Fabric Reinforced Cementitious Matrix (FRCM) systems for masonry strengthening,” *Composites Part B: Engineering,* vol. 70, pp. 215-230, 2015.

[31] A. D'Ambrisi, L. Feo and F. Focacci, “Experimental and analytical investigation on bond between Carbon-FRCM materials and masonry,” *Composites Part B: Engineering,* vol. 46, pp. 15-20, 2013.

[32] G. P. Lignola, C. Caggegi, F. Ceroni, S. De Santis, P. Krajewski, P. B. Lourenço, M. Morganti, C. C. Papanicolau, C. Pellegrino, A. Prota and L. Zuccarino, “Performance assessment of basalt FRCM for retrofit applications on masonry,” *Composites Part B: Engineering,* vol. 128, pp. 1-18, 2017.

[33] F. G. Carozzi, A. Bellini, T. D'Antino, G. de Felice, F. Focacci, L. Hojdys, L. Laghi, E. Lanoye, F. Micelli, M. Panizza and C. Poggi, “Experimental investigation of tensile and bond properties of Carbon-FRCM composites for strengthening masonry elements,” *Composites Part B: Engineering,* vol. 128, pp. 100-119, 2017.

[34] C. Caggegi, F. G. Carozzi, S. De Santis, F. Fabbrocino, F. Focacci, L. Hojdys, E. Lanoye and L. Zuccarino, “Experimental analysis on tensile and bond properties of PBO and aramid fabric reinforced cementitious matrix for strengthening masonry structures,” *Composites Part B: Engineering,* vol. 127, pp. 175-195, 2017.

[35] M. Leone, M. A. Aiello, A. Balsamo, F. G. Carozzi, F. Ceroni, M. Corradi, M. Gams, E. Garbin, N. Gattesco, P. Krajewski, C. Mazzotti, D. Oliveira, C. Papanicolau, G. Ranocchiai, F. Roscini and D. Saenger, “Glass fabric reinforced cementitious matrix: Tensile properties and bond performance on masonry substrate,” *Composites Part B: Engineering,* vol. 127, pp. 196-214, 2017.

[36] M. Santandrea, G. Quartarone, C. Carloni and X. L. Gu, “Confinement of Masonry Columns with Steel and Basalt FRCM Composites,” *Key Engineering Materials,* vol. 747, pp. 342-349, 2017.

[37] L. H. Sneed, F. Ravazdezh, M. Santandrea and I. A. O. Imohamed, "A study of the compressive behavior of concrete columns confined with SRP jackets using digital image analysis.," *Composite Structures,* vol. 179, pp. 195-207, 2017.

[38] M. Santandrea, G. Daissè, C. Mazzotti and C. Carloni, “An Investigation of the Debonding Mechanism between FRCM Composites and a Masonry Substrate,” *Key Engineering Materials,* vol. 747, pp. 382-389, 2017.

[39] M. Santandrea, I. A. O. Imohamed, C. Carloni, C. Mazzotti, S. de Miranda and F. Ubertini, “A study of the debonding mechanism in steel and basalt FRCM-masonry joints,” in *Brick and Block Masonry: Proceedings of the 16th International Brick and Block Masonry Conference, Padova, Italy, 26-30 June 2016*, Padova, 2016.

[40] S. De Santis, F. Ceroni, G. de Felice, M. Fagone, B. Ghiassi, A. Kwiecien, G. P. Lignola, M. Morganti, M. Santandrea, M. R. Valluzzi and A. Viskovic, “Round Robin Test on tensile and bond behaviour of Steel Reinforced Grout systems,” *Composites Part B: Engineering,* vol. 127, pp. 100-120, 2017.

[41] A. Razavizadeh, B. Ghiassi and D. V. Oliveira, “Bond behavior of SRG-strengthened masonry units: Testing and numerical modeling,” *Construction and Building Materials,* vol. 64, pp. 387-397, 2014.

[42] G. de Felice, S. De Santis, L. Garmendia, B. Ghiassi, P. Larrinaga, P. B. Lourenço, D. V. Oliveira, F. Paolacci and C. G. Papanicolaou, “Mortar-based systems for externally bonded strengthening of masonry,” *Materials and structures,* vol. 47(12), pp. 2021-2037, 2014.

[43] C. Carloni, "Analyzing bond characteristics between composites and quasi-brittle substrates in the repair of bridges and other concrete structures.," in *Advanced Composites in Bridge Construction and Repair.*, Sawston, Cambridge, Woodhead Publishing Limited, 2014, pp. 61-93.

[44] F. Focacci, T. D'Antino, C. Carloni, L. H. Sneed and C. Pellegrino, "An indirect method to calibrate the interfacial cohesive material law for," *Materials & Design,* vol. 128, pp. 206-217, 2017.

[45] CEN, EN 772-1, 2011, "Methods of test for masonry units – Part 1: Determination of compressive strength. A1:2015".

[46] C. Carloni, M. Santandrea and R. Wendner, "An investigation on the "width and size effect" in the evaluation of the fracture energy of concrete.," *Procedia Structural Integrity,* vol. 3, pp. 450-458, 2017.

[47] A. Hillerborg, "The theoretical basis of a method to determine the fracture energy GF of concrete.," *Materials and structures,* vol. 18(4), pp. 291-296, 1985.

[48] M. Elices, V. G. Guinea and J. Planas, "Measurement of the fracture energy using three-point bend tests: Part 3—influence of cutting the P-δ tail.," *Materials and Structures,* vol. 25(6), pp. 327-334, 1992.

[49] C. G. Hoover and Z. P. Bažant, "Comprehensive concrete fracture tests: size effects of types 1 & 2, crack length effect and postpeak.," *Engineering Fracture Mechanics,* vol. 110, pp. 281-289, 2013.

[50] DIN 18555-9:1999-09, "Testing of mortars containing mineral binders - Part 9: Hardened mortars; determination of the mortar compressive strength in the bed joint".

[51] J. Henzel and S. Karl, “Determination of strength of mortar in the joints of masonry by compression tests on small specimens,” *Darmstadt Concrete,* vol. 2(1), pp. 123-136, 1987.

[52] Kerakoll S.p.A., “www.kerakoll.com,” [Online]. [Accessed November 2017].

[53] CEN, EN 1015-11:1999, “Methods of test for mortar for masonry – Part 11: Determination of flexural and compressive strength of hardened mortar. A1:2006”.

[54] C. Carloni, M. Santandrea and I. A. O. Imohamed, “Determination of the interfacial properties of SRP strips bonded to concrete and comparison between single-lap and notched beam tests.,” *Engineering Fracture Mechanics,* vol. 186, pp. 80-104, 2017.

[55] C. Carloni, S. Verre, L. H. Sneed and L. Ombres, "Loading rate effect on the debonding phenomenon in fiber reinforced cementitious matrix-concrete joints.," *Composites Part B: Engineering,* vol. 108, pp. 301-314, 2017.

[56] J. Dai, T. Ueda and Y. Sato, “Unified analytical approaches for determining shear bond characteristics of FRP-concrete interfaces through pullout tests” Journal of Advanced Concrete Technology, vol. 4(1), pp. 133-145, 2006.

[57] F. Focacci and C. Carloni, “Periodic variation of the transferable load at the FRP-masonry interface,” *Composite Structures*, vol. 129, pp. 90-100, 2015.

[58] C. Carloni and F. Focacci, "FRP-masonry interfacial debonding: An energy balance approach to determine the influence of the mortar joints," *European Journal of Mechanics-A/Solids*, vol. 55, pp. 122-133, 2016.